Role of the LiPF 6 Salt for the Long-Term Stability of Silicon Electrodes in Li-Ion Batteries – A Photoelectron Spectroscopy Study

6 AUTHORS, INCLUDING:

Bertrand Philippe
Uppsala University
15 PUBLICATIONS **247** CITATIONS

SEE PROFILE

Rémi Dedryvère
Université de Pau et des Pays de l'Adour
60 PUBLICATIONS **1,549** CITATIONS

SEE PROFILE

Mihaela Gorgoi
Helmholtz-Zentrum Berlin
102 PUBLICATIONS **1,226** CITATIONS

SEE PROFILE

K. Edström
Uppsala University
215 PUBLICATIONS **4,224** CITATIONS

SEE PROFILE

Article

Role of the LiPF$_6$ Salt for the Long-Term Stability of Silicon Electrodes in Li-Ion Batteries − A Photoelectron Spectroscopy Study

Bertrand Philippe,[†,‡,⊥] Rémi Dedryvère,*[,†,⊥] Mihaela Gorgoi,[§] Håkan Rensmo,[∥,⊥] Danielle Gonbeau,[†,⊥] and Kristina Edström*[,‡,⊥]

[†]IPREM/ECP (UMR 5254), University of Pau, Hélioparc, 2 av. Pierre Angot, 64053 Pau cedex 9, France

[‡]Department of Chemistry-Ångström Laboratory, Uppsala University, Box 538, SE-75121 Uppsala, Sweden

[§]Helmholz-Zentrum Berlin für Materialien und Energie GmbH, 12489 Berlin, Germany

[∥]Department of Physics and Astronomy, Uppsala University, P.O. Box 530, SE-75121 Uppsala, Sweden

[⊥]Alistore - European Research Institute, 33 rue Saint-Leu, 80039 Amiens cedex, France

ABSTRACT: Silicon presents a very high theoretical capacity (3578 mAh/g) and appears as a promising candidate for the next generation of negative electrodes for Li-ion batteries. An important issue for the implementation of silicon is the understanding of the interfacial chemistry taking place during charge/discharge since it partly explains the capacity fading usually observed upon cycling. In this work, the mechanism for the evolution of the interfacial chemistry (reaction of surface oxide, Li−Si alloying process, and passivation layer formation) upon long-term cycling has been investigated by photoelectron spectroscopy (XPS or PES). A nondestructive depth resolved analysis was carried out by using both soft X-rays (100−800 eV) and hard X-rays (2000−7000 eV) from two different synchrotron facilities. The results are compared with those obtained with an in-house spectrometer (1486.6 eV). The important role played by the LiPF$_6$ salt on the stability of the silicon electrode during cycling has been demonstrated in this study. A partially fluorinated species is formed upon cycling at the outermost surface of the silicon nanoparticles as a result of the reaction of the materials toward the electrolyte. We have shown that a similar species is also formed by simple contact between the electrolyte and the pristine electrode. The reactivity between the electrode and the electrolyte is investigated in this work. Finally, we also report in this work the evolution of the composition and covering of the SEI upon cycling as well as proof of the protective role of the SEI when the cell is at rest.

KEYWORDS: lithium-ion batteries, silicon, alloy, SEI, XPS, PES, synchrotron
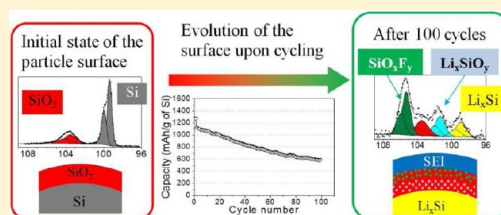
1. INTRODUCTION

The development of portable electronic devices and the increasing need for efficient energy storage systems have motivated the development of lithium-ion (Li-ion) battery technology. Since the battery was first brought to the market in 1991 by Sony,[1] a lot of efforts have been taken to enhance the performance in terms of improved reversible capacity, energy density, power and safety. Furthermore there are new electrode materials and electrolytes coming up as possible replacements for the commercially used graphite (negative electrode) and cobalt containing layered transition metal oxides (positive electrode).

In the search for new negative electrode materials that can replace carbonaceous materials (such as graphite), metals and semimetals mainly found in group 13 and 14 of the periodic table of elements have attracted a special interest due to their ability to electrochemically form alloys with lithium (e.g., Si, Ge, Sn, Sb, etc.). The advantage is the high volumetric and gravimetric capacities and low working potential vs Li$^+$/Li that can be obtained.[2] Among these elements, silicon appears to be the best candidate for the next generation of batteries. Silicon can accommodate 3.75 Li atoms per Si atom at room temperature, resulting in a maximum capacity of 3579 mAh/g (8340 mAh/cm^3) which can be compared to the theoretical capacity of

graphite, 372 mAh/g (818 mA/cm^3). Silicon is also a light, abundant, and cheap material; it represents the second most abundant element in the earth's crust after oxygen.[3]

However, the main drawback is the large volume expansion occurring when lithium reacts to form the alloy. This leads to strong mechanical degradation of the electrode with loss of electrical contact between silicon, the conductive additive (carbon black), and the current collector.[4] The result is an electrode with electrically isolated active particles which can explain the low Coulombic efficiency and the decrease in capacity usually observed for these systems.

Several strategies have been considered to avoid or limit the effect of this expansion and to improve the stability during cycling of the Si-based electrode,[5] for example by reducing the size of the particles,[6] by using specific cycling conditions of the battery,[7] (C-rate, cutoff voltage, and precycling), or by using nanostructured Si materials such as nanotubes,[8−10] nanowires,[11,12] or even more complex structures.[13,14] A lot of work has been carried out on electrode formulation, with the use of

new binders like carboxymethylcellulose sodium salt (CMC),[15,16] poly(acrylic acid) (PAA),[16,17] poly(vinyl alcohol) (PVA),[18] or natural polysaccharide alginate,[19] and important improvements of electrochemical performances have been obtained. Hence silicon is considered today as a credible alternative as negative electrode material.

There are other limitations due to the risk of unwanted side reactions at the electrode/electrolyte interfaces in the Li-ion battery and particularly due to the formation of the solid electrolyte interphase (SEI). A stable SEI is recognized as one of the key parameters for a successful and safe Li-ion battery. For silicon electrodes, the formation of SEI is affected by cracks due to the volume expansion/contraction during cycling. This may consume an extra amount of lithium and electrolyte components which can contribute to the irreversible capacity.

The role of electrode/electrolyte interfacial reactivity for the electrochemical stability of silicon has attracted less attention than for carbonaceous electrodes. Chan et al.[20] analyzed the composition and morphology of the SEI formed on silicon nanowires by X-ray photoelectron spectroscopy (XPS or PES) and scanning electron microscopy (SEM). The morphology of the SEI was reported to be voltage dependent with a thicker SEI at low potential and a partial dissolution and cracking during the delithiation, but the composition of the SEI was consistent with that observed on graphite electrodes. Several strategies were developed to avoid cracking of the SEI, like encapsulation of silicon within a rigid outer shell impermeable to electrolyte solvent molecules but permeable to lithium, in carbon nanotubes for example.[21] But still now the SEI issues have not been resolved, and a better understanding of the processes occurring at interfaces during the first lithium insertion/extraction and during long-term cycling is necessary for the design of a successful silicon-containing Li-ion battery.

In a previous work,[22] we have investigated the surface phenomena occurring during the first electrochemical cycle of a Si/C/CMC composite electrode. The SEI is mainly formed at the beginning of the first discharge, and its composition is very similar to the SEI formed at the surface of carbonaceous[23] electrodes or Sn or Sb-based intermetallic electrodes.[24−26] Its thickness increases with lowering of the electrochemical potential. At the same time, lithium reacts with the silicon nanoparticles. Reaction with the surface SiO_2 layer leads to the formation of Li_2O and lithium silicate Li_4SiO_4, and reaction with bulk silicon leads to the formation of the Li−Si alloy. During the first delithiation, the thickness of the SEI decreases slightly without any significant changes of its composition.

In the present work, we follow how the reaction of the surface oxide, Li−Si alloying process, and SEI evolution develop during long-term cycling of the Si/C/CMC composite electrode. To probe the details in the SEI chemical composition of long-cycled Si-electrode we employed photoelectron spectroscopy (PES). It is one of the few techniques that can give detailed chemical information of surface layers that are as thin as 50−100 Å which is the case for the SEI. We carried out a nondestructive depth-resolved analysis where the photon energy is varied instead of using the surface destructive argon ion etching. The electrodes were hence studied by both soft X-ray PES (photon energy hν = 100−800 eV) and hard X-ray photoelectron spectroscopy (HAXPES, hν = 2000−7000 eV) at two different synchrotron facilities (MaxIV Laboratory, Lund, Sweden and Bessy II, Helmholtz Centre, Berlin, Germany) as well as by the use of in-house PES (Al Kα = 1486.6 eV). According to the model developed by Tanuma et al.[27] to calculate the inelastic mean free

path (IMFP) of photoelectrons as a function of their kinetic energy, and considering that 95% of the XPS signal comes from a layer thickness equal to three times the IMFP, the depths of analysis in silicon at the different photon energies used in this work are as follows: 1.8 nm (230 eV), 4.9 nm (690 eV), 9.5 nm (1487 eV), 14 nm (2300 eV), 35 nm (6900 eV).

2. EXPERIMENTAL DETAILS

2.1. Electrochemical Cycling. Silicon electrodes were prepared with a mixture of 80% (wt%) of crystalline silicon powder (∼50 nm, 70−100 m²/g, Alfa Aesar), 12% of the conductive additive carbon black (SuperP, Erachem Comilog), and 8% binder of sodium carboxymethyl cellulose (CMC, M_w = 700.000, DS = 0.9, Sigma Aldrich). A water−ethanol solution ($EtOH/H_2O$, 70/30) was used as solvent for the slurry preparation. The slurry was mixed in a Retsch planetary mill for 60 min and deposited on a 20 μm thick copper foil. It was then dried at 60 °C for 12 h in an oven, and the obtained coating had a thickness of ∼12−13 μm. Circular electrodes (2 cm diameter) were punched out and dried for 8 h at 120 °C in a vacuum furnace inside the argon glovebox (O_2 < 3 ppm, H_2O < 1 ppm). The mass loading of the electrodes was 0.5 mg of Si per cm². Taking into account the first discharge capacity ∼1300 mAh/g of Si, this corresponds to a capacity loading of ∼0.65 mAh/cm².

Electrochemical cells were assembled by stacking the Si/C/CMC composite electrode (working electrode), a lithium foil (counter and reference electrode), and a polymer separator soaked with the electrolyte ($LiPF_6$ at 1 mol/L dissolved in ethylene carbonate/diethyl carbonate with ratio EC/DEC 2/1). Karl Fischer titration showed the water content to be below 10 ppm (the detection limit of the instrument). This assembly was hermetically vacuum-sealed in a polyethylene-coated aluminum bag with attached nickel tabs as current collectors. Electrochemical discharge and charge were carried out with a Digatron BTS-600 testing apparatus under galvanostatic mode. Cells were cycled between 0.12 V and 0.9 V with a current of 700 mA/g of silicon (≈C/5 with C the maximum theoretical capacity 3578 mAh/g). Four precycles were performed prior to standard galvanostatic cycling. In the precycling, the electrodes were discharged to 500, 1000, 1500, and 2000 mAh·g⁻¹ and charged to 0.9 V, respectively.[28] After cycling the voltage was fixed for one hour to allow relaxation of the cell. The cell was then disconnected, and the current connectors were protected with an adhesive tape to avoid short-circuit during transportation.

Before each PES characterization, the silicon electrode was carefully separated from the rest of the battery components in an argon glovebox and washed with dimethyl carbonate (DMC) solvent in three successive baths to remove the electrolyte. For each bath, the electrode was put into 2 mL of ultralow water content DMC in a clean and dry aluminum container, maintaining a mild manual agitation during 1 min. Then the electrode was removed from the container, quickly dried, and mounted on a sample holder for PES analysis.

2.2. Photoelectron Spectroscopy. Careful precautions were taken for all PES experiments in order to avoid moisture/air exposure of samples during transfer. Samples were either transferred directly from the argon glovebox to the (in-house) spectrometer or via a special built stainless steel transfer system used at the synchrotron facility PES end-stations. The stainless steel transfer system was directly connected to the glovebox and subsequently to the introduction chamber of the end-station which allows the transportation of the sample in a glovebox atmosphere and avoiding further air contamination. The binding energy scale was calibrated by the hydrocarbon C 1s peak at 285.0 eV.

2.2.1. In-House PES. In-house PES measurements were carried out with a Kratos Axis Ultra spectrometer, using a focused monochrom-atized Al Kα radiation (hν = 1486.6 eV). For the Ag 3d5/2 line the full width at half-maximum (fwhm) was 0.58 eV under the recording conditions. The analyzed area of the samples was 300 × 700 μm². The pressure in the analysis chamber was around 5.10⁻⁹ mbar. Short-time spectra were recorded before and after each normal long-time experiment and were compared to each other to check that the samples did not suffer from degradation during the measurements. Core peaks were analyzed using a nonlinear Shirley-type background.[29] The peak positions and areas were optimized by a weighted least-squares fitting

B

dx.doi.org/10.1021/cm303399v | *Chem. Mater.* XXXX, XXX, XXX−XXX
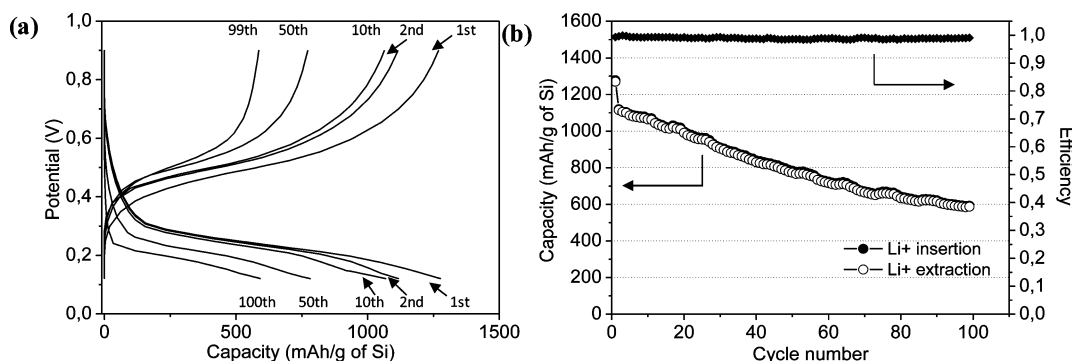
Figure 1. (a) Charge (1st, 2nd, 10th, 50th, and 99th) and discharge (1st, 2nd, 10th, 50th, and 100th) curves of the Si/C/CMC composite electrode vs Li^0 cell between 0.12 and 0.9 V at 700 mA/g of Si. Precycling is excluded. (b) Capacity data and Coulombic efficiency vs cycle number. Precycling is excluded.

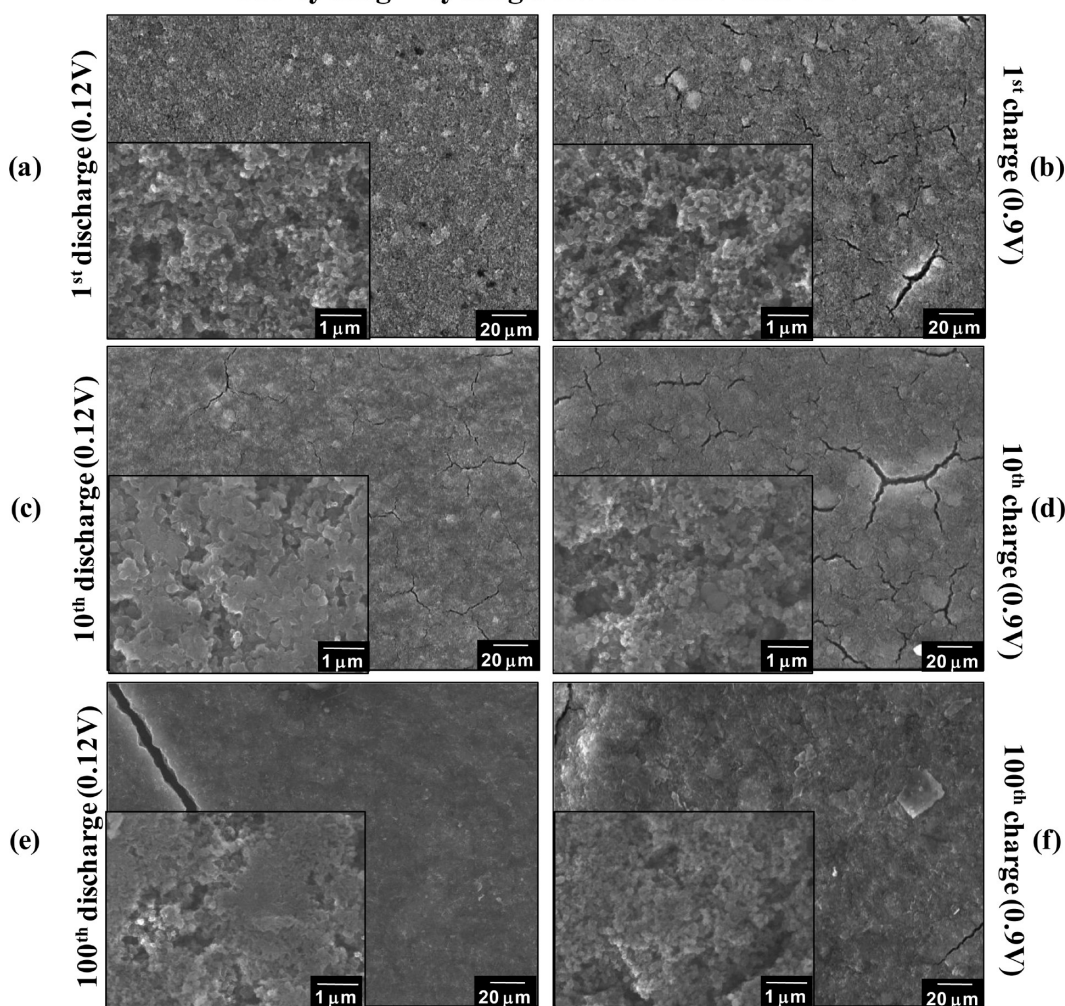## Pre-cycling + cycling between 0.12V and 0.9V

Figure 2. SEM images of the Si/C/CMC composite electrode (20 μm scale horizontal bars and 1 μm scale for inset images): Cycling between 0.12 V and 0.9 V after the 4 steps precycling as described in the Experimental Details section: (a) after 1st discharge and (b) 1st charge, (c) after the 10th discharge and (d) 10th charge, and after (e) 100th discharge and (f) 100th charge.

method using 70% Gaussian, 30% Lorentzian lineshapes. Quantification was performed on the basis of Scofield's relative sensitivity factors.[30]

2.2.2. Soft X-ray PES. Soft X-ray PES measurements were carried out at the MaxIV Laboratory synchrotron facility (I-411 beamline, National Synchrotron Radiation Laboratory, Lund, Sweden), where the usable photon energies range from 50 to 1500 eV. Photons were monochromatized by a Zeiss SX-700 plan grating monochromator.

The photoelectron kinetic energies (K.E.) were measured using a Scienta R4000 WAL analyzer. In order to have the same analysis depth for all spectra measured with soft X-ray, measurements were conducted in such a way that the same photoelectron K.E. was used for all probe elements. In this work, two depths were investigated corresponding to a K.E of 130 and 590 eV. No charge neutralizer was used during the

measurements. The pressure in the analysis chamber was about 10^{-8} mbar.

2.2.3. Hard X-ray PES. Hard X-ray PES measurements were carried out at BESSY II synchrotron facility (HIKE end station,[31] KMC-1 beamline,[32] Helmholtz Zentrum Berlin, Germany), where the usable photon energies range from 2000 to 10000 eV. Fixed excitation energies were used, 2300 and 6900 eV (first order lights from respectively the Si(111) and the Si(422) double-crystal monochromator). For such high photon energies, the difference in probing depth for the probed core levels is minor and has therefore been neglected in the interpretation of the spectra shown in the present investigation. The analyzer was a Scienta R4000 optimized for high kinetic energies up to 10 keV. No charge neutralizer was used, and the pressure was around 10^{-8} mbar in the analysis chamber.

2.3. Scanning Electron Microscopy. The morphology of electrodes was observed by a scanning electron microscopy (SEM) with a JEOL Microprobe JAMP 9500F operating at the probe current of 0.1 nA and 30 keV and a working distance (source/sample) of about 24 mm.

3. RESULTS AND DISCUSSION

3.1. Electrochemical Results. Batteries were submitted to a four step precycling where the initial crystalline structure is slowly transformed into an amorphous phase.[28] Then, the capacity is limited during the standard galvanostatic cycling using a cutoff voltage of 0.12 V. This procedure has several advantages. First the limited capacity leads to the reduction of the volume expansion, and so, the expansion can be accommodated by both the binder and the porosity of the electrode.[7] Second, the limitation of the capacity during the precycling prevents the formation of the crystalline phase $Li_{15}Si_4$ which reduces part of the initial irreversible capacity usually observed after a full discharge.

Figure 1 (a) shows the galvanostatic discharge/charge curves (between 0.12 V and 0.9 V at 700 mA/g of Si) of the 1st, 2nd, 10th, 50th cycle, the 99th charge, and the 100th discharge, and Figure 1 (b) shows the discharge/charge capacities and the Coulombic efficiency (ratio of charge capacity of the nth cycle/ discharge capacity of the nth cycle) as a function of cycle number. The four precycles are not plotted. We can see that after the precycling, the capacity is mainly lost between the 1st and the 2nd cycle ($\sim$150 mAh/g), and then the capacity decreases constantly from $\sim$1100 mAh/g to $\sim$600 mAh/g after 100 cycles. All our tested batteries showed similar behavior. A stable Coulombic efficiency above 98% is obtained as seen in Figure 1b.

Note that the four precycles presented a Coulombic efficiency of $\sim$55%, $\sim$90%, $\sim$95%, and $\sim$97%, respectively. The resulting irreversible capacity is around 400−450 mAh/g of Si after the four precycles which is less than the 550 mAh/g observed after a single cycle employing a full discharge to 0.01 V as reported in our previous work.[22]

3.2. Surface Morphology. Changes in the silicon electrode morphology at different steps of cycling are presented in the SEM images of Figure 2 (a)−(f).

We can clearly see that after one cycle, in contrast with the formation of big cracks upon charge observed after a first full lithiation,[22,33] only a few and quite small cracks are present (Figure 2(b)). This reduction, of number and size of cracks as a result of the capacity limitation, is crucial for good electrode stability and is a strong argument for the use of a limited potential window.

After 10 cycles, the lithiated sample (Figure 2 (c)) shows very small cracks, and no cracks are observed after 100 discharge cycles (Figure 2 (e)) (The big crack observed at the top left in Figure 2 (e) was formed during the sample preparation.). At

higher magnification (inset in Figure 2(e)), it can be observed that after 100 cycles the electrodes have a smooth surface topography as observed in previous work upon cycling.[34] If we look at the delithiated samples, the smooth surface topography is not visible after the 10th (Figure 2 (d)) or the 100th charge (Figure 2 (f)). After 100 cycles, there are no visible cracks. This is probably due to lithium being trapped in the silicon particles that have lost contact with carbon black or with the current collector and become inactive to further cycling. More and more lithium is trapped during cycling which can explain the observed global capacity fading. The inactive lithiated silicon has a swelled shape and prevents the reopening of the cracks at some point. It is to note that the smoothness of the surface is just visible on lithiated samples and not on delithiated samples.

In summary, our study shows fewer and smaller cracks when a cutoff voltage of 0.12 V is used. This feature is mainly explained by the capacity limitation adopted during our electrochemical tests. Capacity limitation allows the porosity of the electrodes to buffer the Si expansion: the cracking is reduced as well as the progressive loss of particle contact as previously reported by Bridel et al.[35]

3.3. PES Study. *3.3.1. Effect of a Long Cycling on the Electrode Surface. 3.3.1.1. SEI Analysis. (a). Covering by the SEI.* Figure 3 shows the total amount of silicon measured (Si 2p
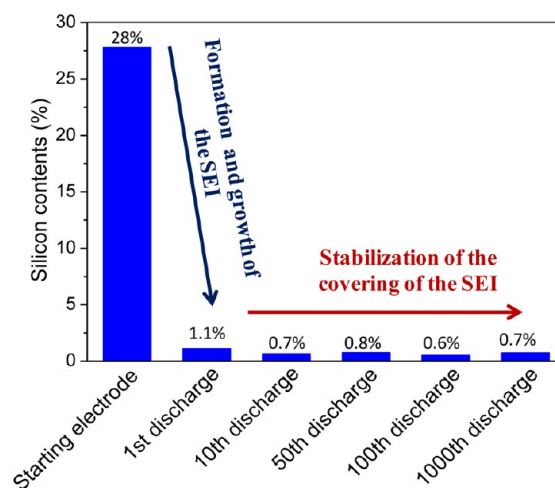

Figure 3. The silicon content at the surface of the electrodes as a function of cycle number (after precycling). The data are based on in-house PES (hν = 1486.6 eV) Si 2p spectra of Si/C/CMC composite electrodes, and the values are given as traditional atomic percentages as described in the Experimental Details section.

spectra) at the surface of the sample after the 1st, 10th, 50th, 100th, and the 1000th discharge down to 0.12 V after the precycling step (hν = 1486.6 eV, analysis depth equal to three times the inelastic mean free path, i.e. $\sim$5−10 nm). The variations in atomic percentages reported in this histogram are an indirect measurement of the SEI thickness at the different cycles. All the phases containing silicon are found to be below the SEI layer containing all the other elements present in our system (C, O, F, P, and Li), so silicon atomic percentages appear as a good indicator for the variation of the SEI thickness. The atomic percentages reported in Figure 3 correspond to the discharged state (lithiated state), where the SEI is thicker than in the delithiated state (charged).[22]

This figure shows a dramatic drop of the Si 2p signal between the starting electrode (28%) and the 1st discharge following the
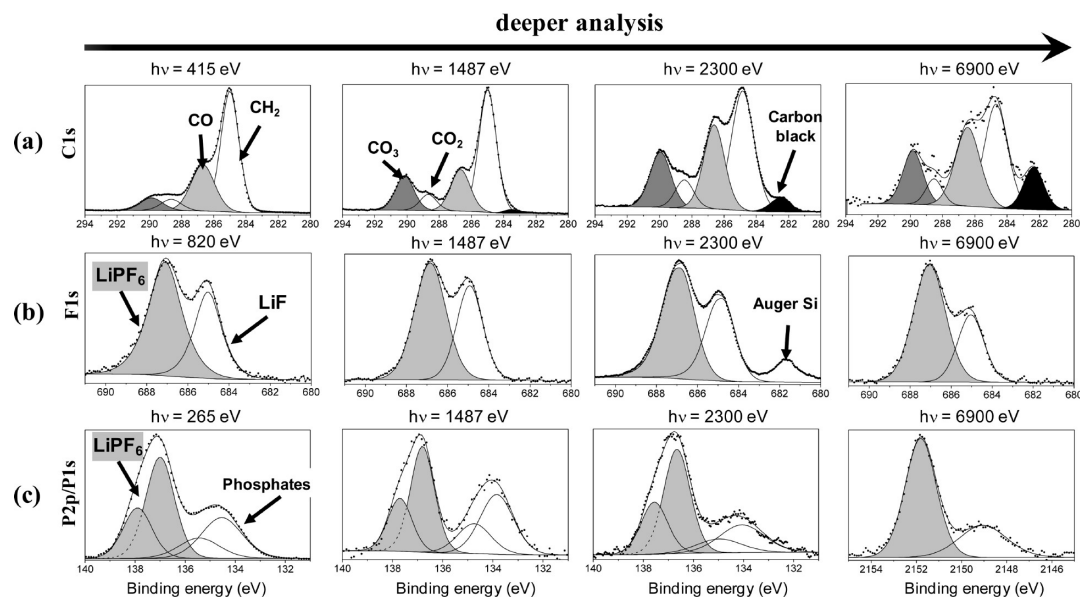
deeper analysis

Figure 4. (a) C 1s, (b) F 1s, and (c) P 2p/P 1s spectra of the Si/C/CMC composite electrodes after the 100th discharge shown as a function of the analysis depth.
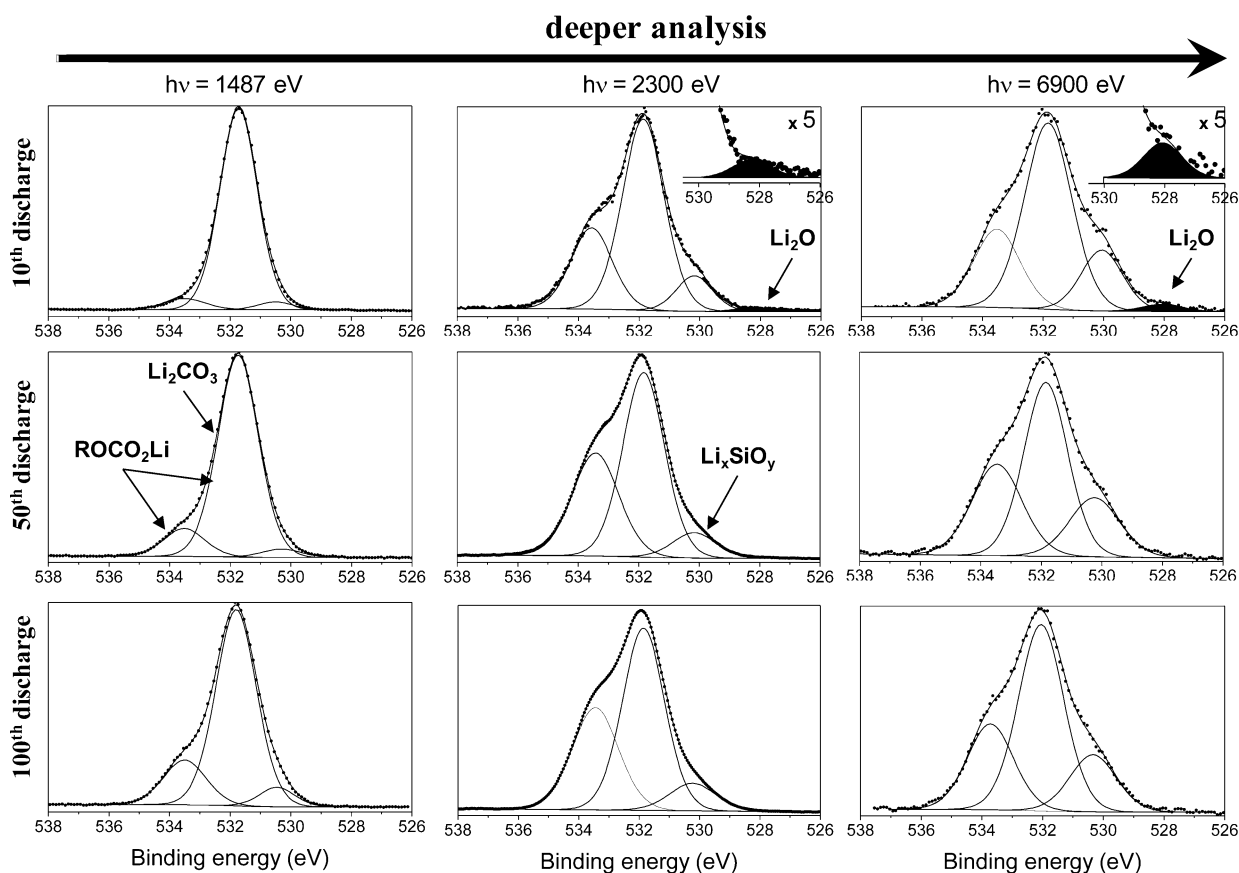
deeper analysis

Figure 5. O 1s spectra of the Si/C/CMC composite electrodes after the 10th, 50th, and 100th discharge. Evolution as a function of the analysis depth.

precycling step (1.1%). Then, after the 10th discharge, the atomic % has decreased to 0.7%. After the 10th cycle, and all the way up to the 1000th discharge, the atomic % stays around 0.6−0.8% showing that the SEI covering of the silicon particles is quite stable during continuous cycling.

(b). Composition. Figure 4 (a) shows C 1s spectra of the Si/C/CMC composite electrode after the 100th discharge as a

function of the photon energy and thus of the analysis depth (hν = 410 eV (MAX IV), 1486.6 eV (in-house PES), 2300 and 6900 eV (BESSY II)). The four main components visible in these four spectra (in white and gray) represent the carbonaceous species deposited at the surface and among them the characteristic peaks corresponding to binding energy values for C−O (286.5 eV), O═C−O (288.5 eV), and CO$_3$ (290 eV) carbon environments.

The 290 eV peak can be assigned to carbonates (Li_2CO_3 and/or lithium alkyl carbonates) present in the SEI. Oxalates and polyethylene oxide (PEO: $(−CH_2−CH_2−O−)_n$) may also be found in the SEI.[36,37] Due to the electrochemical degradation of the solvents present in the electrolyte, these species are commonly found on the surface of other negative electrode materials (e.g., graphite, tin-based electrode), and several mechanisms for their formation have been described in the literature.[36,38−41] The main peak at 285 eV is attributed to hydrocarbon contamination always observed at the surface of a sample by PES, which is confirmed by the predominance of this peak at the lowest analysis depth. It may also be attributed to CH_2-containing species in the SEI. However, no conclusion on the nature of the SEI can be clearly stated based on this component. It can be seen that the ratio of CO_3/CO_2 and of CO_3/CO slightly increases as a function of the analysis depth and especially between $h\nu$ = 410 and 1486.6 eV. This suggests that Li_2CO_3 is found preferably close to the active particle as it was suggested by Edström et al. on a graphite negative electrode.[42] Nevertheless, these ratios remain stable by further increasing the analysis depth, showing the homogeneity of the carbonaceous compounds within the SEI layer, and just the first or the two first nanometers of the SEI extreme surface exhibit some small fluctuations. The same type of behavior is observed for the O 1s spectra (Figure 5) with differences in spectra present at the lowest photon energy and a good conservation of the overall shape of the spectra at higher photon energy.

In the C 1s spectra a fifth surface component appears at low binding energy (∼282−283 eV) at the greatest analysis depth. This peak, assigned to carbon black, gradually increases with increasing photon energy. If we look at the atomic % of carbon black detected in the first 5−10 nm (in-house PES), we can see that the content is very stable (around 0.5%) after the 10th, 50th, and 100th discharges, respectively. The presence of this component confirms the thickness stability of the SEI upon cycling.

The surface elements formed by reduction of the electrolyte salt can provide interesting additional information. Figure 4 (b) shows the F1s spectra of the Si/C/CMC composite electrode after the 100th discharge as a function of the analysis depth. The peak at 685 eV is attributed to lithium fluoride (LiF), whereas the one at 687 eV can be assigned to the $LiPF_6$ salt. After the 1st cycle,[22] $LiPF_6$ was found to be located at the extreme surface of the particles since its intensity decreased as a function of the analysis depth. However, after the 100th discharge, the ratio between LiF and $LiPF_6$ peaks barely changes from one analysis depth to another. Therefore the observed $LiPF_6$ does not result only from traces of salt that were not completely removed after washing with DMC solvent. These results show that $LiPF_6$ forms an integral part of the SEI following diffusion of PF_6^- ions (as Li^+ ions) into the surface layer.

Note that the F 1s spectrum at 2300 eV exhibits an extra peak at low binding energy (∼681.7 eV); this peak corresponds to a Si Auger peak (the $KL_{2,3}L_{2,3}$ transition occurs with a kinetic energy of ∼1618 eV).

The evolution of the P 2p/P 1s peak as a function of the analysis depth is shown in Figure 4 (c). The high photon energy provided at BESSY II ($h\nu$ = 6900 eV) allows us to record the P 1s (binding energy ∼2150 eV) core peak. P 1s gives similar information as can be obtained by P 2p. However at high photon energies, the cross section of P 1s exceeds that of P 2p, allowing for a better signal/noise ratio and a more efficient measurement. The spectra consist of two peaks: a first one at 137 eV (P 2p)/

2152 eV (P 1s) (in gray) attributed to the salt $LiPF_6$ and a second at 134 eV (P 2p)/ 2149 eV (P 1s) (in white) assigned to phosphates which are commonly found in SEI layers using similar electrolytes. As previously, we can notice that the ratio between the two peaks barely changes, so the PF_6^- ions are part of the SEI after 100 cycles.

Fluorine and phosphorus core peaks have a very stable signature as a function of the analysis depth, and the presence of LiF and phosphates is found to be homogeneously distributed within the SEI layer.

3.3.1.2. Evolution of the Surface Oxide. The O 1s spectra of the Si/C/CMC composite electrode after the 10th, 50th, and 100th discharge are shown in Figure 5, as a function of analysis depth. After the 1st discharge, various oxygenated species are formed on the particle surfaces and in the SEI layer. Their specific signatures are in a narrow binding energy range, so a precise interpretation of the O 1s spectra is complex. However, we can see that after 10, 50, and 100 cycles, the O 1s spectra are rather similar to the ones obtained after a single discharge.[22] The component with the maximum intensity has a binding energy around 532 eV for all the analysis depths, and there is also a component at higher binding energy (∼533.5 eV). These two signatures are in good agreement with carbonates, alkyl carbonates, and other organic species commonly found in SEI with carbonates solvents.[23,43] The component at ∼530−530.5 eV is attributed to the lithium silicate Li_4SiO_4.

First, if we examine Figure 5 and the evolution of spectra during cycling with three different photon energies (from the top to the bottom), the stability of the SEI is noticeable by the conservation of the overall shape of the two main components at high binding energy. Moreover, the stability in thickness is demonstrated by the overall stability of the ratio between the signatures of Li_4SiO_4 (which is below the SEI layer) and the oxygenated peaks within the SEI.

Second, at a given state of discharge, if we compare data at 2300 and 6900 eV, we can see that the SEI oxygenated species are stable. In contrast, the proportion of Li_4SiO_4 increases when using higher photon energy since this compound is buried underneath the SEI layer.

Finally, the O 1s peaks indicate that the SEI is homogeneous in composition and thickness during cycling, and this is especially demonstrated with the analysis of the data from the greatest analysis depths (2300 and 6900 eV) which means that the part of the SEI closest to the electrode materials is very stable. Small fluctuations are, however, visible at the lowest depths ($h\nu$ = 1486 eV).

In the measurements with largest analysis depth performed after the 10th discharge, an additional barely visible peak with a low specific binding energy (at 528 − 528.5 eV, black in Figure 5) is detectable and can be assigned to lithium oxide Li_2O. In the charged state, no peak could be detected at this binding energy. It is well-known that a reaction of lithium with silicon oxide can occur for nanosized particles and that this leads to the reduction of the surface oxide according to the following reaction:[44]

$$SiO_2 + 4Li \rightarrow Si + 2Li_2O \tag{1}$$

We have shown[22] that Li_2O was formed during the 1st discharge and that its formation was reversible upon the 1st cycle. The spectra in Figure 5 allow us to say that the formation of Li_2O is reversible at least during the 10th 1st cycles but that the amount of Li_2O is decreasing upon cycling. Indeed, its peak intensity is very low after the 10th discharge and just visible with a photon energy of 2300 and 6900 eV, whereas this component was

detected with an in-house PES ($h\nu$ = 1486.6 eV) after the 1st discharge. After 50 and 100 discharges, Li_2O is not detected anymore in any of the O 1s spectra suggesting a consumption of this species. This point will be discussed later.

3.3.1.3. Evolution of Si Compounds. (a). Lithium Insertion/ Extraction upon Cycling. Our detailed PES study of the interfacial phenomena occurring upon the first discharge/charge cycle[22] has revealed the irreversible formation of a lithium silicate compound: Li_4SiO_4, by reaction of the lithium with the silicon dioxide present at the surface of the Si nanoparticles. At the same time, the formation of the Li−Si alloy during the first lithium insertion process has been clearly illustrated.

Figure 6 shows the in-house PES Si 2p spectra of the Si/C/ CMC composite of the pristine electrode (Figure 6 (a)) and after
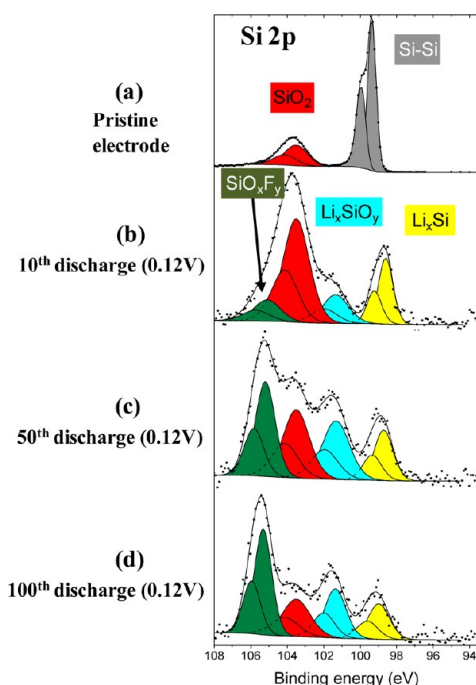

Figure 6. Si 2p spectra (in-house PES, 1486.6 eV) of the Si/C/CMC composite electrode: (a) of the pristine electrode and after (b) the 10th discharge at 0.12 V, (c) the 50th discharge at 0.12 V, and (d) the 100th discharge at 0.12 V. The four steps precycling and the high C-rate were applied for (b), (c), and (d) samples.

the 10th, 50th, and 100th discharges at 0.12 V preceded by four precycles (in Figure 6 (b)−(e), respectively).

A thin SiO_2 layer (Si $2p_{3/2}$ at 103.5 eV, red in Figure 6) is detected beside bulk silicon (Si $2p_{3/2}$ at 99.5 eV, gray in Figure 6) on the pristine electrode. After the 10th discharge, four silicon-containing phases are observed: SiO_2; lithium silicate[22] (Si $2p_{3/2}$ at 101.3 eV, blue color); the component at low binding energy assigned to the Li_xSi alloy (Si $2p_{3/2}$ at 98.5−99 eV, yellow color); and a fourth component at high binding energy (Si $2p_{3/2}$ at 105− 106 eV, green color). The high binding energy of this latter component allows us to assign it to a fluorinated or more probably to a partially fluorinated species SiO_xF_y.[45−47] If we look at the quantification, no additional information can be provided from the other core peaks. The fourth component of the Si2p spectra represents less than 0.2% of the signal of the in-house PES analysis, and the F1s or O1s core peaks are mostly the signature of the SEI so a signature of SiO_xF_y cannot be identified

from these peaks. The nature and origin of this phase will be discussed later.

After the 50th and 100th discharge (Figure 6 (d) and (e)), the same four components are identified as after the 10th discharge. Upon cycling, we can clearly observe a significant increase of the amount of the fluorinated Si species even if the lithium silicate and the silicon oxide formed during the first lithiation are still present after 100 cycles.

(b). Evolution of the Si2p Spectrum after 100 Discharges As a Function of the Analysis Depth. In this part, we focus the discussion on the SiO_xF_y component appearing and growing upon cycling.

The PES analysis depth can be modified by varying the photon energy of the incident beam used for the analysis. An increase of the photon energy leads to the increase of the kinetic energy of the ejected photoelectrons. Since the inelastic mean free path of the photoelectrons is highly dependent on their kinetic energy, it leads to a change of the PES analysis depth.

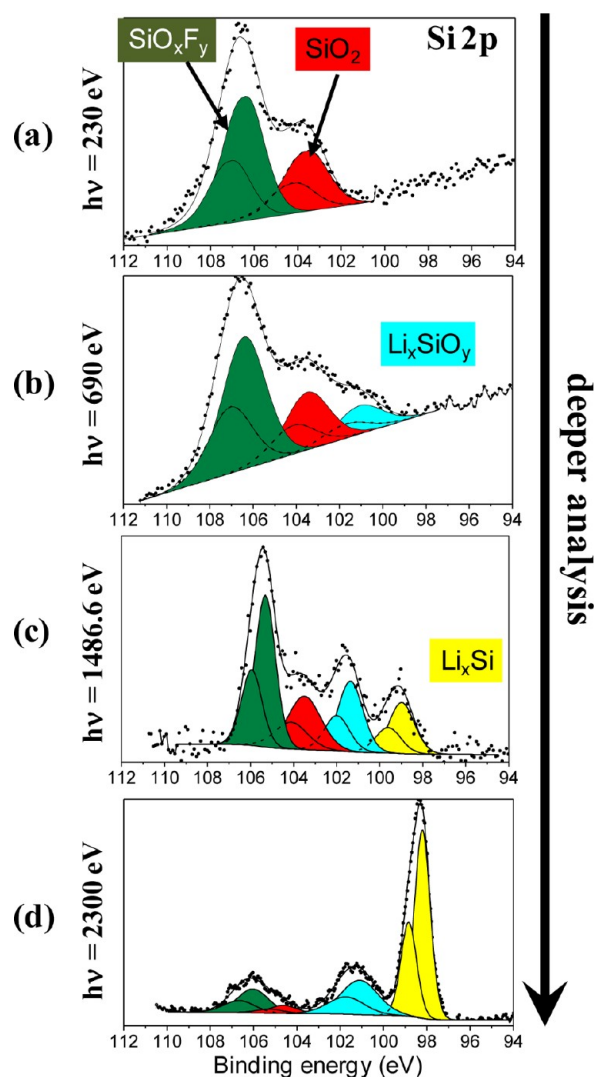Figure 7 shows the Si 2p spectrum of Si/C/CMC composite electrode after the 100th discharge and its dependence on the

Figure 7. Si 2p spectra of the Si/C/CMC composite electrode after the 100th discharge as a function of the analysis depth. (a) $h\nu$ = 230 eV (MAX IV), (b) $h\nu$ = 690 eV (MAX IV), (c) $h\nu$ = 1486.6 eV (in-house PES), (d) $h\nu$ = 2300 eV (BESSY II).

photon energy (hν). In Figure 7 (a), we can see that when a lower photon energy is used (hν = 230 eV, outermost surface), only two components are observed: the component assigned to a fluorinated environment of the silicon at ~106 eV and the silicon dioxide at ~103.5 eV (in green and red, respectively in Figure 7 (a)). The lithium silicate component appears when a higher photon energy is used (hν = 690 eV, deeper into the surface, blue in Figure 7 (b)). The appearance of the Li$_x$Si alloy (yellow in Figure 7 (c)) is finally visible when an in-house PES (hν = 1486.6 eV) is used, and it becomes the major component at the greatest analysis depth (hν = 2300 eV, Figure 7 (d)). At the highest photon energy (looking through the surface into the bulk), the surface species, i.e. SiO$_x$F$_y$, SiO$_2$, and Li$_4$SiO$_4$ show a lower intensity than the Li$_x$Si alloy.

Note that some binding energy shifts and broadening effects are observed from one spectrum to another. This is due to the fact that the spectra obtained at the synchrotrons (hν = 230 eV, 690 and 2300 eV) were recorded without any charge neutralization system. Indeed, during the PES experiment, the emission of photoelectrons entails a loss of negative charge at the surface. For good electronic conductors, this charge loss is easily balanced due to the electrical connection of the sample to a common ground with the spectrometer. However, this charge compensation is not always sufficient without any charge neutralizer, leading to some broadening of the peaks. Moreover, when a sample is made up of mixed conducting and insulating compounds, which is the case here, it is commonly observed that the signals of different compounds are shifted one to another (differential charging effect).[48]

Nevertheless the different components are very well recognizable, and this depth-evolution of the Si 2p spectra allows us to conclude that the fluorinated phase is formed at the extreme surface of the silicon nanoparticles. Moreover, this compound is much more a surface phase than the lithium silicate, so it is probably formed onto or by reaction with the top layers of the SiO$_2$ covering the active particles.

(c). Nature of the New Fluorinated Phase - Etching by HF. The previous results strongly suggest that the fluorinated phase formed at the extreme surface of the silicon nanoparticles is due to a process occurring between the particles and the only source of fluorine which is the electrolyte salt LiPF$_6$.

It is well-known that LiPF$_6$ is very sensitive to traces of water, moisture, and alcohol[49,50] and that it leads to the formation of hydrofluoric acid HF (2-3):[23,51,52]

$$LiPF_6 \rightarrow LiF + PF_5 \qquad (2)$$

$$PF_5 + H_2O \rightarrow POF_3 + 2HF \qquad (3)$$
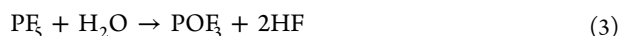
In organic carbonate electrolytes the equilibrium of the process can be shifted to the right due to the interaction between PF$_5$ and solvent molecules. In addition, the liberation of protons during formation of LiF (Li$^+$ + HF $\rightarrow$ LiF + H$^+$) can also increase the rate of the process by an autocatalytic mechanism.[52]

In the present case, the generated HF can react with the native oxide at the surface of the silicon electrode modifying the favorable interactions between the binder and the active material surface.[53,54]

Silica dissolution by HF plays a very important role in many technological fields, and several papers have proposed reaction mechanisms for the etching process of SiO$_2$ in HF solutions.

Based on experimental results, it appears that the dissolution is a surface reaction-controlled process with adsorption of HF and HF$_2^-$, this last species being nearly four to five times more

reactive than HF.[55−57] The catalytic actions of H$^+$ ions has also been pointed out especially for HF solutions of extremely low concentrations.[58]

Ab initio quantum chemical calculations have shown that the etching reaction of SiO$_2$ by HF molecule involves four steps, with each step consisting of an attack on the Si−O bonds by a HF molecule with generation of an Si−F bond.[59]

More recently, Mitra et al.[60] proposed a reaction mechanism for dissolution of silica in HF solutions. It consists of a simple elementary reaction that involves a coordinated attack of the Si−O bond by H$^+$ (electrophilic attack on the bridging oxygen atom) and HF$_2^-$ (nucleophilic attack on the adjacent Si atom) as shown in Figure 8.
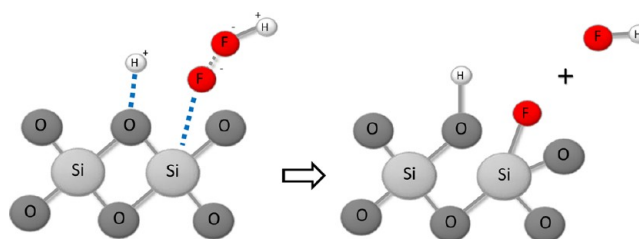

Figure 8. Schematic illustration of the breaking of the Si−O bond as proposed by Mitra et al.[60]

It is unlikely that multiple bonds break simultaneously, so it is expected that the process consists of a series of such elementary reaction steps.

The identification of SiO$_x$F$_y$ species (with $y \leq 3$) at the extreme surface of the particles as evidenced by the variation in analysis depth (Figure 7) is consistent with this proposition.

These results suggest that the reaction of HF with SiO$_2$ in a battery is more complex than the catalytic reaction pathway previously proposed[61] with direct formation of volatile SiF$_4$ by etching of the SiO$_2$ layer.

In addition, the gradual disappearance of Li$_2$O during cycling previously observed (Figure 5) can be put in parallel with the gradual appearance of the fluorinated silicon species. Li$_2$O can easily react with hydrofluoric acid (HF) and form LiF.[62]

$$Li_2O + HF \rightarrow LiF + H_2O \qquad (4)$$

The formation of water in reaction 4 allows the regeneration of HF. Both the consumption of Li$_2$O and the formation of the fluorinated species are enhanced during cycling.

Note that no involvement of the binder was evidenced in the mechanism of attack of the SiO$_2$ layer by HF. Moreover, other binders showing an interest for silicon electrodes (like PAA or alginate for example) present the same kind of organic functions (hydroxyl and carboxyl functional groups) as CMC. Therefore no influence of the nature of the binder is expected on these results.

3.3.2. Reactivity of the Pristine Electrode with the Electrolyte. In order to probe the reactivity of the pristine electrode with the electrolyte, an additional experiment has been carried out. The electrode was mounted in half-cells, as previously, but without any electrochemical cycling, and the evolution of the chemical composition in the surface was followed as a function of storage time.

Figure 9 shows the Si 2p core peak of the pristine Si/C/CMC electrode after contact with the electrolyte during 2, 96, and 244 days. The electrode was then washed with DMC before analysis.
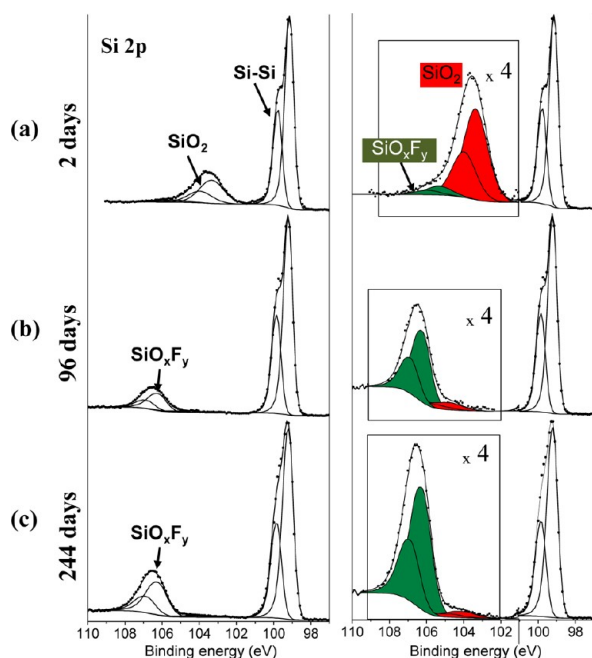
Figure 9. Evolution of Si 2p spectra (in-house PES, 1486.6 eV) of the pristine Si/C/CMC electrode after contact with the electrolyte during (a) 2 days, (b) 96 days, and (c) 244 days. A zoom of the higher binding energy region is shown on the right-hand side.

After two days (Figure 9 (a)), we can observe two main components assigned to bulk silicon (Si $2p_{3/2}$ at ∼99.5 eV) and silicon dioxide (Si $2p_{3/2}$ at ∼103.5 eV). An additional phase is already appearing at higher binding energy (weak intensity at ∼105−106 eV), corresponding to the fluorinated compound. After 96 and 244 days, a strong decrease of the silicon dioxide component is observed, and the intensity of the fluorinated

compound increases. Moreover, we can see that the fluorinated compound slightly shifts toward higher binding energy (Si $2p_{3/2}$ at ∼106 eV) suggesting an increased fluorination of the compound.

These trends are in agreement with the earlier described etching process, and it is a clear evidence that SiO_2 is reacting with the electrolyte as a function of storage time.

3.3.3. Formation of the Fluorinated Compound: The Important Role of the SEI Layer. We have shown that the fluorinated compound appears not only upon cycling but also after a simple contact with the electrolyte. In both cases, HF is involved, but the kinetics of the reaction is quite different which is reflected in the surface chemistry obtained in the presence or absence of the SEI.

Figure 10 (a) shows the evolution of the Si 2p spectra of the Si/C/CMC electrode upon cycling and/or upon soaking in the electrolyte. Compared to the Si 2p core peak of the pristine electrode (① in Figure 10) a clear evolution of the Si 2p core peak (② in Figure 10) is observed after 96 days of storage with the electrolyte. The native oxide layer (SiO_2 peak in red) has almost disappeared, and a fluorinated compound which covers the bulk silicon is identified (in green in Figure 10, ②).

The spectrum ③ (Figure 10) shows the Si 2p core peak after a 1st partial discharge (up to 500 mAh/g of Si). At this state, we know that the SEI is mainly formed, silicon is lithiated (Li_xSi in yellow), and lithium silicate (in blue) is formed into the SiO_2 layer.[22] The interesting point is that after a first discharge, even after a contact of 182 days with the electrolyte, no fluorinated compounds appears. This feature points out the protective role of the SEI. Once it is formed, the SEI behaves like a barrier prohibiting the HF acid to reach the oxide layer. However, during cycling (when a potential is applied), this barrier allows the migration of the acid, the etching of the silicon dioxide can occur, and the fluorinated compound is formed at the interface between
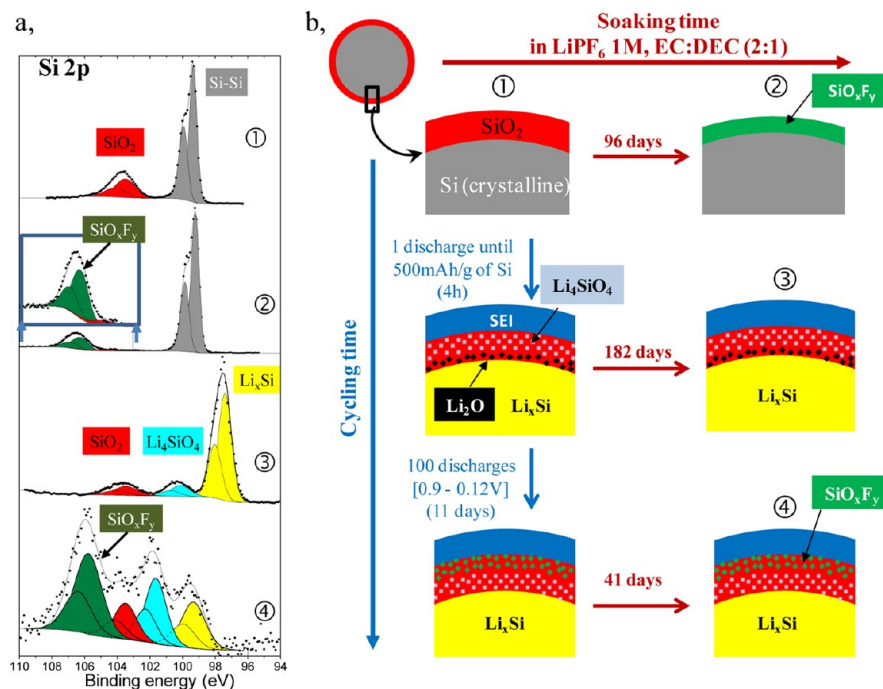

Figure 10. a, Si 2p spectra (in-house PES, 1486.6 eV) (1) of the Si/C/CMC pristine electrode, (2) of a pristine electrode in contact 96 days with the electrolyte, (3) after a first discharge until 500 mAh/g of Si, (4) after the 100th discharge at 0.12 V (with precycling) (to the left). b, Schematic view of the compounds formed on the silicon particle surfaces during cycling and/or during storage with the electrolyte (to the right).

the SEI and the remaining oxide layer (④ in Figure 10). When the potential is stopped, no further reactions are expected, since the SEI regains its protective role.

4. CONCLUSION

By the original use of depth-resolved PES based on the use of different X-ray photon energies on a Si/C/CMC composite electrode together with SEM investigations, we have demonstrated valuable information on the role of the $LiPF_6$ salt for the chemistry of the silicon electrode during cycling. We have followed the chemistry occurring at the surface of Si nanoparticles in addition to its high influence on the SEI chemical composition. We have also illustrated the crucial importance of how the cycling procedure influences the overall surface morphology of the electrode.

The adopted capacity limitation (cutoff potential of 0.12 V) results in the reduction of the amount of cracks formed in the electrode during lithium extraction. As a consequence, less electrolyte and lithium ions are lost by reconstruction and/or a constant growth of the SEI.

When the SEI has been formed (mainly during the 1st discharge), its chemical composition and its covering properties are stable during the subsequent cycling of the electrode. The chemical composition seems to be quite homogeneous within the SEI layer especially considering the inorganic compounds (LiF, $LiPF_6$, phosphates). Some fluctuations at the extreme surface of the SEI are noticed for the organic part (oxygenated and carbonaceous components).

In the analysis of the surface of the active particles, a fluorinated silicon species $(SiO_xF_y, y \leq 3)$ appears during cycling at the interface between the Si particles and the SEI. This phase also appears by simple contact of the electrolyte with a pristine electrode upon time. Combining these observations and literature data, it is possible to explain the formation of such a phase pointing out the important role of HF resulting from $LiPF_6$ degradation. The Li_2O phase is present only in the lithiated state, and it slowly disappears upon cycling, which may also be an effect of HF.

Beyond this, a better understanding of the detrimental role of HF in Li-ion batteries using silicon electrodes has been obtained, and we can expect further improvements using other electrolyte salts.

■ AUTHOR INFORMATION

Corresponding Author
*E-mail: remi.dedryvere@univ-pau.fr (R.D.), kristina.edstrom@kemi.uu.se (K.E.).

Notes
The authors declare no competing financial interest.

■ ACKNOWLEDGMENTS

■ REFERENCES

(1) Nagaura, T.; Tozawa, K. *Prog. Batteries Sol. Cells* **1990**, *9*, 209−217.
(2) Larcher, D.; Beattie, S.; Morcrette, M.; Edstrom, K.; Jumas, J.-C.; Tarascon, J.-M. *J. Mater. Chem.* **2007**, *17*, 3759−3772.
(3) *Shriver & Atkins' Inorganic Chemistry*, 5th ed.; Oxford University Press: 2010.
(4) Chen, Z.; Christensen, L.; Dahn, J. R. *Electrochem. Commun.* **2003**, *5*, 919−923.
(5) Zhang, W.-J. *J. Power Sources* **2010**, *196*, 13−24.
(6) Kasavajjula, U.; Wang, C.; Appleby, A. J. *J. Power Sources* **2007**, *163*, 1003−1039.
(7) Obrovac, M. N.; Krause, L. J. *J. Electrochem. Soc.* **2007**, *154*, A103−A108.
(8) Wu, H.; Chan, G.; Choi, J. W.; Ryu, I.; Yao, Y.; McDowell, M. T.; Lee, S. W.; Jackson, A.; Yang, Y.; Hu, L.; Cui, Y. *Nat. Nanotechnol.* **2012**, *7*, 310−315.
(9) Evanoff, K.; Khan, J.; Balandin, A. A.; Magasinski, A.; Ready, W. J.; Fuller, T. F.; Yushin, G. *Adv. Mater.* **2012**, *24*, 533−537.
(10) Park, M.-H.; Kim, M. G.; Joo, J.; Kim, K.; Kim, J.; Ahn, S.; Cui, Y.; Cho, J. *Nano Lett.* **2009**, *9*, 3844−3847.
(11) Chen, H.; Dong, Z.; Fu, Y.; Yang, Y. *J. Solid State Electrochem.* **2009**, *14*, 1829−1834.
(12) Chan, C. K.; Peng, H.; Liu, G.; McIlwrath, K.; Zhang, X. F.; Huggins, R. A.; Cui, Y. *Nat. Nanotechnol.* **2008**, *3*, 31−35.
(13) Wu, H.; Zheng, G.; Liu, N.; Carney, T. J.; Yang, Y.; Cui, Y. *Nano Lett.* **2012**, *12*, 904−909.
(14) Liu, N.; Wu, H.; McDowell, M. T.; Yao, Y.; Wang, C.; Cui, Y. *Nano Lett.* **2012**, *12*, 3315−3321.
(15) Lestriez, B.; Bahri, S.; Sandu, I.; Roué, L.; Guyomard, D. *Electrochem. Commun.* **2007**, *9*, 2801−2806.
(16) Bridel, J. S.; Azaïs, T.; Morcrette, M.; Tarascon, J. M.; Larcher, D. *Chem. Mater.* **2010**, *22*, 1229−1241.
(17) Magasinski, A.; Zdyrko, B.; Kovalenko, I.; Hertzberg, B.; Burtovyy, R.; Huebner, C. F.; Fuller, T. F.; Luzinov, I.; Yushin, G. *ACS Appl. Mater. Interfaces* **2010**, *2*, 3004−3010.
(18) Park, H.-K.; Kong, B.-S.; Oh, E.-S. *Electrochem. Commun.* **2011**, *13*, 1051−1053.
(19) Kovalenko, I.; Zdyrko, B.; Magasinski, A.; Hertzberg, B.; Milicev, Z.; Burtovyy, R.; Luzinov, I.; Yushin, G. *Science* **2011**, *334*, 75−79.
(20) Chan, C. K.; Ruffo, R.; Hong, S. S.; Cui, Y. *J. Power Sources* **2009**, *189*, 1132−1140.
(21) Hertzberg, B.; Alexeev, A.; Yushin, G. *J. Am. Chem. Soc.* **2010**, *132*, 8548−8549.
(22) Philippe, B.; Dedryvère, R.; Allouche, J.; Lindgren, F.; Gorgoi, M.; Rensmo, H.; Gonbeau, D.; Edström, K. *Chem. Mater.* **2012**, *24*, 1107−1115.
(23) Leroy, S.; Blanchard, F.; Dedryvère, R.; Martinez, H.; Carré, B.; Lemordant, D.; Gonbeau, D. *Surf. Interface Anal.* **2005**, *37*, 773−781.
(24) Naille, S.; Dedryvère, R.; Zitoun, D.; Lippens, P. E. *J. Power Sources* **2009**, *189*, 806−808.
(25) Ehinon, K. K. D.; Naille, S.; Dedryvère, R.; Lippens, P. E.; Jumas, J. C.; Gonbeau, D. *Chem. Mater.* **2008**, *20*, 5388−5398.
(26) Stjerndahl, M.; Bryngelsson, H.; Gustafsson, T.; Vaughey, J. T.; Thackeray, M. M.; Edström, K. *Electrochim. Acta* **2007**, *52*, 4947−4955.
(27) Tanuma, S.; Powell, C. J.; Penn, D. R. *Surf. Interface Anal.* **1991**, *17*, 911−926.
(28) Li, J.; Lewis, R. B.; Dahn, J. R. *Electrochem. Solid-State Lett.* **2007**, *10*, A17−A20.
(29) Shirley, D. A. *Phys. Rev. B* **1972**, *5*, 4709−4714.
(30) Scofield, J. H. *J. Electron Spectrosc. Relat. Phenom.* **1976**, *8*, 129−137.
(31) Gorgoi, M.; Svensson, S.; Schäfers, F.; Öhrwall, G.; Mertin, M.; Bressler, P.; Karis, O.; Siegbahn, H.; Sandell, A.; Rensmo, H.; Doherty, W.; Jung, C.; Braun, W.; Eberhardt, W. *Nucl. Instrum. Methods Phys. Res., Sect. A* **2009**, *601*, 48−53.
(32) Schaefers, F.; Merlin, M.; Gorgoi, M. *Rev. Sci. Instrum.* **2007**, *78*, 123102.
(33) Beaulieu, L. Y.; Eberman, K. W.; Turner, R. L.; Krause, L. J.; Dahn, J. R. *Electrochem. Solid-State Lett.* **2001**, *4*, A137−A140.
(34) Wang, W.; Moni Kanchan, D.; Prashant, N. K. *J. Mater. Chem.* **2007**, *17*, 3229−3237.
(35) Bridel, J. S.; Azais, T.; Morcrette, M.; Tarascon, J. M.; Larcher, D. *J. Electrochem. Soc.* **2011**, *158*, A750−A759.

(36) Verma, P.; Maire, P.; Novák, P. *Electrochim. Acta* **2010**, *55*, 6332−6341.

(37) Dedryvère, R.; Laruelle, S.; Grugeon, S.; Gireaud, L.; Tarascon, J. M.; Gonbeau, D. *J. Electrochem. Soc.* **2005**, *152*, A689−A696.

(38) Peled, E. *J. Electrochem. Soc.* **1979**, *126*, 2047−2051.

(39) Aurbach, D.; Daroux, M. L.; Faguy, P. W.; Yeager, E. *J. Electrochem. Soc.* **1987**, *134*, 1611−1620.

(40) Andersson, A. M.; Edstrom, K. *J. Electrochem. Soc.* **2001**, *148*, A1100−A1109.

(41) Andersson, A. M.; Herstedt, M.; Bishop, A. G.; Edström, K. *Electrochim. Acta* **2002**, *47*, 1885−1898.

(42) Edström, K.; Herstedt, M.; Abraham, D. P. *J. Power Sources* **2006**, *153*, 380−384.

(43) Dedryvère, R.; Gireaud, L.; Grugeon, S.; Laruelle, S.; Tarascon, J. M.; Gonbeau, D. *J. Phys. Chem. B* **2005**, *109*, 15868−15875.

(44) Saint, J.; Morcrette, M.; Larcher, D.; Laffont, L.; Beattie, S.; Pérès, J. P.; Talaga, D.; Couzi, M.; Tarascon, J. M. *Adv. Funct. Mater.* **2007**, *17*, 1765−1774.

(45) Chuang, T. J. *J. Appl. Phys.* **1979**, *51*, 2614−2619.

(46) Ram, P.; Singh, J.; Ramamohan, T.; Venkatachalam, S.; Sundarsingh, V. *J. Mater. Sci.* **1997**, *32*, 6305−6310.

(47) Pereira, J.; Pichon, L. E.; Dussart, R.; Cardinaud, C.; Duluard, C. Y.; Oubensaid, E. H.; Lefaucheux, P.; Boufnichel, M.; Ranson, P. *Appl. Phys. Lett.* **2009**, *94*, 071501.

(48) Cazaux, J. C. *J. Electron Spectrosc. Relat. Phenom.* **2010**, *178−179*, 357−372.

(49) Heider, U.; Oesten, R.; Jungnitz, M. *J. Power Sources* **1999**, *81−82*, 119−122.

(50) Campion, C. L.; Li, W.; Lucht, B. L. *J. Electrochem. Soc.* **2005**, *152*, A2327−A2334.

(51) Aurbach, D.; Markovsky, B.; Shechter, A.; Ein-Eli, Y.; Cohen, H. *J. Electrochem. Soc.* **1996**, *143*, 3809−3820.

(52) Plakhotnyk, A. V.; Ernst, L.; Schmutzler, R. *J. Fluorine Chem.* **2005**, *126*, 27−31.

(53) Hochgatterer, N. S.; Schweiger, M. R.; Koller, S.; Raimann, P. R.; Wohrle, T.; Wurm, C.; Winter, M. *Electrochem. Solid-State Lett.* **2008**, *11*, A76−A80.

(54) Munao, D.; van Erven, J. W. M.; Valvo, M.; Garcia-Tamayo, E.; Kelder, E. M. *J. Power Sources* **2010**, *196*, 6695−6702.

(55) Judge, J. S. *J. Electrochem. Soc.* **1971**, *118*, 1772−1775.

(56) Spierings, G. A. C. M. *J. Mater. Sci.* **1993**, *28*, 6261−6273.

(57) Liang, D.-T.; Readey, D. W. *J. Am. Ceram. Soc.* **1987**, *70*, 570−577.

(58) Kikuyama, H.; Waki, M.; Miyashita, M.; Yabune, T.; Miki, N.; Takano, J.; Ohmi, T. *J. Electrochem. Soc.* **1994**, *141*, 366−374.

(59) Hoshino, T.; Nishioka, Y. *J. Chem. Phys.* **1999**, *111*, 2109−2114.

(60) Mitra, A.; Rimstidt, J. D. *Geochim. Cosmochim. Acta* **2009**, *73*, 7045−7059.

(61) Lux, S. F.; Lucas, I. T.; Pollak, E.; Passerini, S.; Winter, M.; Kostecki, R. *Electrochem. Commun.* **2011**, *14*, 47−50.

(62) Shiraishi, S.; Kanamura, K.; Takehara, Z.-i. *Langmuir* **1997**, *13*, 3542−3549.